Core Spreading Vortex Method for Simulating 3D Flow around Bluff Bodies

Lavi R. Zuhal[1], Duong V. Dung[1], Alex J. Sepnov[2] & Hari Muhammad[1]

[1]Faculty of Mechanical and Aerospace Engineering, Bandung Institute of Technology, Jalan Ganesha No. 10, Indonesia,
[2]Department of Mechanical Engineering, Keio University, YAGAMI/Yokohama/Kanagawa, Japan
Email: lavirz@ae.itb.ac.id

Abstract. This paper presents the development of the core spreading vortex element method, a mesh-free method for simulating 3D viscous flow over bluff bodies. The developed method simulates external flow around complex geometry by tracking local velocities and vorticities of particles introduced within the fluid domain. The viscous effect is modeled using the core spreading method coupled with a splitting spatial adaption scheme and a smoothing interpolation scheme for overlapping issues and population control, respectively. The particle's velocity is calculated using the Biot-Savart formulation. To accelerate computation, the fast multipole method (FMM) is employed. The solver was validated using a number of benchmark problems for both unbounded and bounded flows at low Reynolds numbers. For unbounded cases, simulation of the collision of two vortex rings was performed. The energy spectrum calculated using the current core spreading diffusion model approached that of the particle strength exchange model. To test the performance of the method in simulating bounded flow problems, simulation of flow around a sphere was carried out. The results were found to be in very good agreement with those reported in the literature.

Keywords: *bluff body flow; core spreading; fast multipole method; viscous flow; vortex method.*

1 Introduction

Problems of flow around bluff bodies have attracted a lot of interest in the past few decades [1-4]. The distinguishing feature of bluff body flows in real fluids is the generation of vorticity and the shedding of vortices into the wake, which is difficult to predict using an analytical approach. Due to the current availability of high performance computers, these problems can now be overcome using numerical methods known as computational fluid dynamics (CFD).

In CFD, there are two main approaches: grid-based and meshless methods. As suggested by the name, in the more traditional grid-based methods, the Navier-

Received November 27th, 2013, Revised September 26th, 2014, Accepted for publication October, 24th, 2014.
 ISSN: 2337-5779, DOI: 10.5614/j.eng.technol.sci.2014.46.4.7

Stokes equations are solved using a discretized grid. However, simulation of flow over for example a deformable body is very difficult, if not impossible, using the grid-based CFD. In particular, the difficulty is due to the requirement to generate a grid at every time step because of the continuous change in the geometry of the body.

On the other hand, meshless methods, such as smoothed particle hydrodynamics (SPH) [5] and vortex element methods [6,7], benefit from their inherent adaptivity. Specifically, meshless or Lagrangian methods use Lagrangian grid points, which follow the movement of the flows. Therefore, such methods can handle irregular and complex geometries without any complication.

As far as complex vortical flow is concerned, a vortex element method is the suitable solver to resolve the vorticity region correctly with a high resolution [3,8]. In addition, another advantage of this type of method is that it can be easily implemented in parallel computation in order to allow long time simulations.

Accordingly, a fully meshfree version of the vortex element method (VEM) was developed in this research in order to simulate 3D viscous flow problems. The fast multipole method (FMM) was employed to accelerate the computation of the developed method. A novel spatial adaptation scheme was introduced to control the computational resolution and particle population. Finally, the performance of the developed method was investigated by performing benchmark simulations for unbounded and bounded flow: a simulation of two colliding vortex rings and a simulation of flow around a sphere, respectively.

2 Vortex Element Method

For unsteady incompressible viscous flow with uniform density ρ and kinematic viscosity ν, the momentum equations for the flow field, are written as

$$\frac{\partial \underline{u}}{\partial t} + (\underline{u}.\nabla)\underline{u} = -\frac{1}{\rho}\nabla p + \nu\nabla^2\underline{u} \tag{1}$$

In Eq. (1), $\underline{u}$is the velocity vector and $p$is the pressure of the flow field. By taking the curl $(\nabla\times)$ of Eq. (1) and defining the vorticity vector as $\underline{\omega} = \nabla \times \underline{u}$ we get the vorticity-velocity equations:

$$\frac{d\underline{\omega}}{dt} = (\underline{\omega}.\nabla)\underline{u} + \nu\nabla^2\underline{\omega} \tag{2}$$

with a Dirichlet boundary condition of $\underline{u} = 0$. It is common to use a time-splitting algorithm over a time step $[t, t + \Delta t]$, to numerically integrate the

nonlinear system. This time-splitting algorithm basically solves Eq. (2) in two fractional steps. First, the stretching part of the equation is solved by evaluating

$$\frac{d\underline{\omega}}{dt} = (\underline{\omega}.\nabla)\underline{u} \tag{3}$$

withno-flow-through boundary condition$\underline{u}.\underline{n} = 0$, where$\underline{n}$is the normal vector at the boundary. The vorticity field at the end of this stretching process is updated as $\underline{\omega}^{str}$. This vorticity is then used to initialize the vorticity for the second step, where the viscous part is worked out by solving

$$\frac{\partial\underline{\omega}}{\partial t} = \nu\nabla^2\underline{\omega} \tag{4}$$

with full no-slip boundary conditions $\underline{u} = 0$. The vorticity at the end of the diffusion process is consistent with that obtained directly from the momentum Eq. (2).

2.1 Treatment of Viscous Effect

Due to the linearity of Eq. (4), the viscous part on the right hand side can be split into two parts. The first part is valid within the fluid domain (solution denoted by $\underline{\omega}^f$), while the second part is valid in regions close to solid boundaries (solution denoted by $\underline{\omega}^b$). These equations are expressed as

$$\begin{cases} \frac{\partial\underline{\omega}^f}{\partial t} = \nu\nabla^2\underline{\omega}^f \\ \underline{\omega}^f(t = t_n) = \underline{\omega}^{str} \\ \underline{\omega}^f \in \Omega \end{cases} \tag{5}$$

$$\begin{cases} \frac{\partial\underline{\omega}^b}{\partial t} = \nu\nabla^2\underline{\omega}^b \\ \underline{\omega}^f(t = t_n) = \underline{\omega}_{wall}, \partial\Omega \\ \frac{\partial\underline{\omega}}{\partial\underline{n}} = \frac{1}{\nu}\frac{\underline{\gamma}_\Omega}{\Delta t} \end{cases} \tag{6}$$

In these equations $\partial\Omega$ and Ω denote the boundary and the fluid domain, respectively. While it is easy to solve Eq. (5) using standard schemes (particle strength exchange or core spreading), Eq. (6) is subjected to boundary conditions. The boundary conditions are given in terms of velocity, which is translated into wall vorticity $\underline{\Gamma}_{wall}$, which will be discussed in more detail in Subsection 2.3.

In vortex methods, the fluid domain is represented by particles. Each particle is tracked by calculating its vortex strength ($\underline{\Gamma}$), core radius (σ), and velocity ($\underline{u}$).

The viscous effect is modeled by changing either $\underline{\Gamma}$, σ, or $\underline{u}$.

The analytical solution of the diffusion Eq. (5) is

$$\underline{\omega_i} = \frac{\Gamma_i}{(2\pi\sigma^2)^{\frac{3}{2}}} exp(-\frac{r_{ij}^2}{2\sigma^2}) \tag{7}$$

$\underline{r_{ij}}$ is the distance between the vortex element j and vortex element i. σ is the core size of the vortex blob which is obtained by setting it as the variance of the Gaussian distribution kernel

$$\sigma^2 = 2\nu\Delta t \tag{8}$$

where Δt is the time scale to resolve the viscous flow.

2.1.1 Particle Strength Exchange

The particle strength exchange (PSE) method exchanges the particle's strength in a supported domain by approximating the Laplacian operator on the right-hand side of Eq. (5) by integral operator as

$$\nabla^2\omega = \frac{2}{\sigma^2}\int G\left(\frac{|\underline{x}-\underline{y}|}{\sigma}\right)[\omega(\underline{y}) - \omega(\underline{x})]dy \tag{9}$$

The kernel $G\left(\frac{|\underline{x}-\underline{y}|}{\sigma}\right)$ in this expression is a particle distribution function defined as

$$G\left(\frac{|\underline{x}-\underline{y}|}{\sigma}\right) = \frac{1}{(2\pi)^{3/2}} exp(-\frac{|\underline{x}-\underline{y}|^2}{2\sigma^2}) \tag{10}$$

By employing (9), (5) can be expressed as

$$\frac{d\Gamma_i}{dt} = 2\nu\sum_{j=1}^{N}\frac{1}{\sigma_{ij}^2}G\left(\frac{|\underline{x_i}-x_j|}{\sigma}\right)(\sigma_i^3\Gamma_j - \sigma_j^3\Gamma_i) \tag{11}$$

σ_{ij} is the average core size between particle i and particle j. The supported domain mentioned earlier is defined as 5σ from $\underline{x_i}$ [9]. In this work, the PSE diffusion model was used for comparison purposes.

2.1.2 Core Spreading Method

The core spreading method (CSM) models the viscous effect by spreading the core size of every single particle with respect to time. The rate of change of the core radius is calculated using

$$\frac{d\sigma_i}{dt} = \frac{\nu}{\sigma_i} \tag{12}$$

This is a straightforward procedure to increase the core radius of the vortex blob, which actually represents the viscous diffusion process.

However, the core size will eventually become too large to retain the local fluid velocity, as mentioned in Greengard [10]. Barba [6] and Yokota [11] have proposed an alternative method, based on the use of radial basis function interpolation to redistribute the vorticity strengths field using the smaller core sizes. The method leads to a linear system $\varsigma_{ij}\Gamma_i = \omega_i$ where ς_{ij} is a Gaussian function of two vortex elements i and j,ω_i is the vorticity of the element i evaluated by Eq. (7). The first advantage of this method is that the number of particles will remain constant during computation. The second advantage is that overlapping among the vortex elements is spatially adapted by reducing the core sizes to become sufficiently small.

Rossi [12,13] proposed a splitting scheme in which the "father" blob is split into the several smaller "children" blobs if the core radius of the vortex blob is larger than a certain threshold. Meanwhile, the vortex strength of these child blobs isthe father blob's strength divided by the number of child blobs. The core radius of the child blobs is reset to a smaller value. Obviously, the children's cores are overlapped after this process.

In this study, the splitting scheme proposed by Rossi [13] for unbounded flow simulation (vortex ring simulation) and external bounded flow simulation is extended to 3D cases. Since the splitting scheme introduces a large amount of error, there is a need to carefully consider the core radius threshold and the splitting scheme itself. Another issue is that the use of the splitting scheme introduces a large amount of vortex elements, more than those required to resolve the flow. Thus, in the following section, a remeshing scheme employing cubic spline interpolation is proposed for the purpose of controlling the population of vortex elements after a splitting event. In addition, this interpolation also serves as a means to control the overlapping among vortex elements, which is important in high-resolution simulation.

2.1.3 Spatial Adaptation Schemes

2.1.3.1 Splitting Scheme

In order to control the size of the blobs, Rossi, Huang, *et al*. [14] limited the blob size to a maximum core width σ_{max}. The splitting scheme splits a parent vortex ofcore width σ_0 and strength Γ_0 into M smaller vortices, whenever σ_0 is greater than σ_{max}. Then, the width of each "child" vortex is set as $\alpha\sigma_0$, where

$0 < \alpha < 1$. With this setting, the larger value of αinduces a smaller error due to the splitting scheme ($\alpha = 0.9$ was chosen in this study). The child vortices are uniformly distributed around the center of the parent vortex at distance r. The value of$r$ and the strength (Γ_c) of the child vortices are determined by preserving the total circulation and the second moment of vorticity about the center of the parent vortex, as shown in Figure 1.

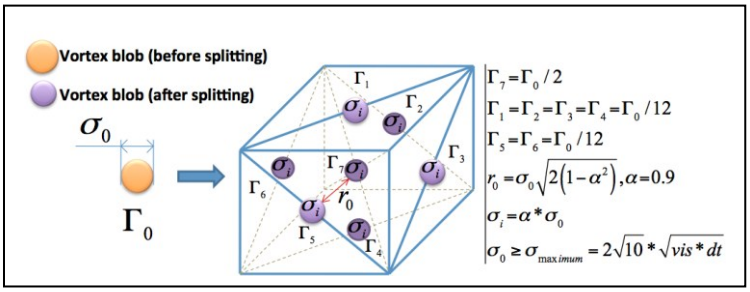

Figure 1 Splitting scheme with one weakened parent vortex (yellow circle) surrounded by six child vortexes (purple circle).

2.1.3.2 M_4' Interpolation Scheme

In order to maintain a sufficient amount of vortex elements to resolve the flow while still maintaining the overlapping among the vortex elements, Barba [6] proposed another spatial adaptation scheme for the core spreading method. This spatial adaptation scheme is a cubic spline interpolation called M_4', which conserves angular momentum, linear impulse and energy. This scheme is also used to redistribute the vortex elements and interpolate their strength, Γ, within the whole fluid domain. In 1D cases, the M_4' interpolation is simply expressed as:

$$M_4'(X) = \begin{cases} \frac{1}{2}(2 - 5X^2 + 3X^3), & 0 \leq X \leq 1 \\ \frac{1}{2}(1 - X)(2 - X^2)^2, & 1 \leq X \leq 2 \\ 0, & otherwise \end{cases} \tag{13}$$

where the grid size h is set to be $h = \alpha\sigma_0$.

As shown in Figure 2, X is the distance between the particle and the grid node, normalized by h. The fraction of the particle information, which is attributed to the grid node, or vice versa, is carried by $M_4'(X)$. In 2D and 3D cases, tensor products are used to express the M_4'interpolation. In this work, a splitting spatial adaptation scheme is combined with the M_4' redistribution interpolation in one time step in order to control the particle population and overlapping.

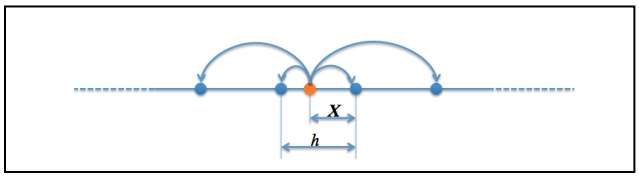

Figure 2 Illustration of the stencil width of the M_4'redistribution interpolation scheme for 1D cases. The interpolation redistributes the vortex strength of the vortex elements to the grid nodes.

2.2 Fast Multipole Method

The Biot-Savart law is used to calculate the velocity field $\underline{u}(\underline{x}_p, t)$. The original formulation of Biot-Savart is written as an integral over the vorticity support, which is approximated as a summation over all of the particles:

$$\underline{u}(\underline{x}, t) = \frac{1}{4\pi}\sum_{i=1}^{N_p} \frac{\underline{\Gamma}_i \times (\underline{x} - \underline{x}_i)}{\sigma^3 |\underline{x} - \underline{x}_i|} + \nabla\phi \tag{14}$$

This summation requires anO(N^2) type of operation, known as the "N-body problem". Greengard and Rokhlin [15] have proposed the fast multipole method (FMM) to accelerate N-body computation, based on the use of multipole expansion. First, particles are grouped into tree structures of cubes. Next, the cubes exchange moments using multipole expansions instead of evaluating the direct particle pair interactions:

$$\underline{u}_p(\underline{x}, t) = \sum_{n=0}^{\infty}\sum_{m=-n}^{n} \nabla\left(\frac{Y_n^m(\theta,\phi)}{r^{n+1}}\right) \times \left\{\sum_p \rho_p^n Y_n^{-m}(\alpha_p, \beta_p)\underline{\Gamma}_p\right\} \tag{15}$$

Also, the particle strength is evaluated as

$$\underline{\Gamma}_p(\underline{x}, t) = \sum_{n=0}^{\infty}\sum_{m=-n}^{n} \alpha_q . \nabla\left(\frac{Y_n^m(\theta,\phi)}{r^{n+1}}\right) \times \left\{\sum_p \rho_p^n Y_n^{-m}(\alpha_p, \beta_p)\underline{\Gamma}_p\right\} \tag{16}$$

Accordingly, the FMM operations reduce the computational cost from N^2 to N log N.

2.3 No-through Boundary Condition

Bounded flow problems require the enforcement of the no-through boundary condition. The vortex element method is a meshfree approach. Therefore, the enforcement of the no-through boundary condition was accomplished through the use of the boundary element method (BEM). The BEM calculates a vortex sheet's strength, which represents the slip velocity on the boundary necessary to satisfy the no-through condition. In BEM, the boundary is discretized into linear panels and the vortex strength of each panel Γ_{panel} is calculated. These vortex strengths or wall circulations represent the initial vorticity vectors on the wall

panels. The calculated vortex strength is a vector with two wall-tangent components and a normal component that satisfy the no-through condition.

2.4 No-slip Boundary Condition

In the vortex method there is a direct relation between the no-through and the no-slip boundary conditions, called the linked boundary condition, as depicted in Figure 3.

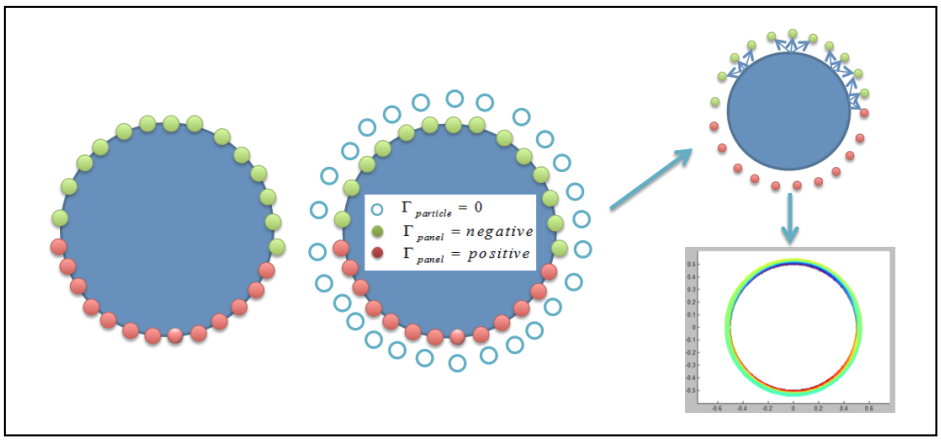

Figure 3 Enforcement of no-slip boundary condition. The vortex strengths of wall panels will be diffused to the near-wall vortex blobs.

Basically, it can be shown that the no-slip boundary condition is automatically satisfied when the no-through boundary condition is fulfilled. The process of translating the vorticity from the panels (computed using BEM) to the particles is explained by Kamemoto [8] and sketched in Figure 4.

Specifically, the procedure involves the introduction of nascent vortex elements that model the boundary layer surrounding the wall. As shown in this figure, these vortex elements are distributed along the boundary with a predetermined height that depends on the kinematic viscosity and time step. Next, the nascent vortex elements are converted into vortex plates, which have volume V_{vor} and strength Γ_{panel}. Finally, the vortex plates are replaced by vortex blobs with the same volume and strength. These blobs are then shed like other existing particles. At this point, the wall boundary conditions have been satisfied and a new set of particles is created.

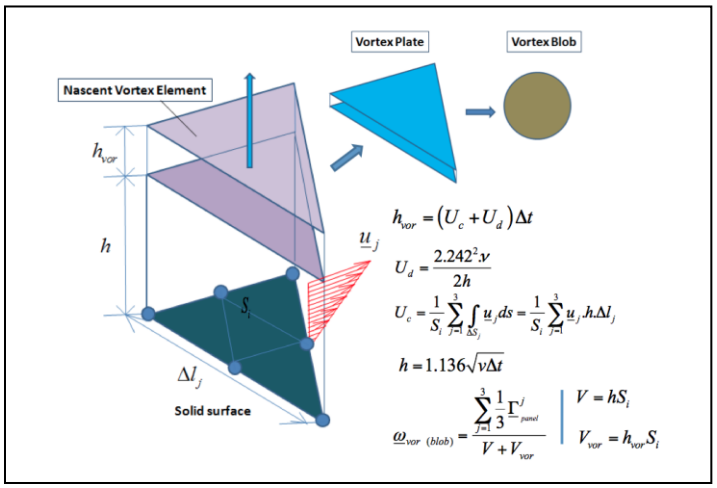

Figure 4 Enforcement of no-slip boundary condition. The vortex blobs will be generated based on the vortex strength and slip velocity of the wall panels calculated using BEM.

3 Simulations and Discussions

3.1 Collision of Vortex Rings

A simulation of colliding vortex rings was conducted in order to test the performance of the developed code in simulating unbounded flows. In particular, this benchmark simulation can demonstrate the ability of the diffusion model in capturing the details of the reconnection process. 3D CSM was utilized for the simulation. The results were compared with results from a similar successful simulation conducted using PSE and results from a similar simulation carried out by Chatelain [16]. Figure 5 depicts an upper vortex ring

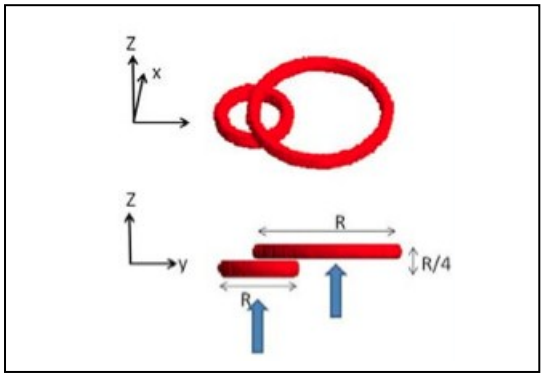

Figure 5 Configuration of the simulation of vortex ring in Re=250.

with radius *R* and a lower vortex ring with radius *R*/2. The lower ring is placed with its center located at the radius of the first ring separated and moved over a distance of *R*/4 in the y-direction. Instead of the two rings moving in opposite directions, both rings move in the same upward direction.

The parameters used for these simulations (both CSM and PSE) are listed in Table 1.

Table 1 Parameters for the vortex ring simulation.

	CSM	**PSE**
Reynolds number (Re)	250	250
Initial vortex strength (Γ_0)	1	1
Time step (Δt)	0.025	0.025
Kinematic viscosity ($\nu = 1/\mathrm{Re}$)	0.004	0.004
Radius of ring (R)	1	1
Vorticity limitation ($\nu.3\mathrm{e}-04$)	$1.2\mathrm{e}-06$	$1.2\mathrm{e}-06$
Initial core size ($\sigma_{\mathrm{init}} = \sqrt{2\nu\Delta t}$)	0.014	none
Maximum core size ($\sigma_{\max} = 10.\sigma_{\min}$)	0.14	0.14

It is well known that vortex methods can successfully calculate the inertia sub-range of the energy spectrum cascade whereby the diffusion model plays an important role in defining the dissipation range in the kinetic energy cascade. In the present work, we focused on the study of the two diffusion models (CSM and PSE) in order to observe their influence on the dissipation range. The kinetic energy and energy spectrum were evaluated at every time step of the simulation. The kinetic energy and energy spectrum depend only on core size and vortex strength of the vortex blobs, as indicated in the following equations:

$$\mathrm{E}_\sigma = \frac{1}{16\pi}\sum_{i,j}\frac{1}{|\underline{x}_i-\underline{x}_j|}\left[2\frac{\rho}{\sqrt{\rho^2+1}}\underline{\Gamma}_i\cdot\underline{\Gamma}_j+\frac{\rho^3}{(\rho^2+1)^{3/2}}\left(\frac{(\underline{x}_i-\underline{x}_j)\cdot\underline{\Gamma}_i(\underline{x}_i-\underline{x}_j)\cdot\underline{\Gamma}_j}{|\underline{x}_i-\underline{x}_j|\quad|\underline{x}_i-\underline{x}_j|}\right)\underline{\Gamma}_i\cdot\underline{\Gamma}_j\right] \quad with\ \rho=|\underline{x}_i-\underline{x}_j|/\sigma \tag{17}$$

$$E(k)=\exp\left(-\frac{(k\rho)^2}{2}\left(\frac{1}{2\pi}\right)^2\sum_i\sum_j\frac{\sin(k|\underline{x}_i-\underline{x}_j|)}{k|\underline{x}_i-\underline{x}_j|}\underline{\Gamma}_i\cdot\underline{\Gamma}_j\right) \quad where\ \ k=\overline{1,2,\ldots,n}\ \ (wave\ number) \tag{18}$$

The kinetic energy results of both the CSM and the PSE simulations are summarized in Figure 6. The results demonstrate that the energy decay ranged from 0.73 to 0.45 (m^2/s^2). At the initial stage of the simulation, the energy spectrums calculated by both the PSE and the CSM method were the same (0.73 m^2/s^2). This is because the initial core sizes of the particles used in both tests were initially set to be the same (σ_{max} in Table 1).

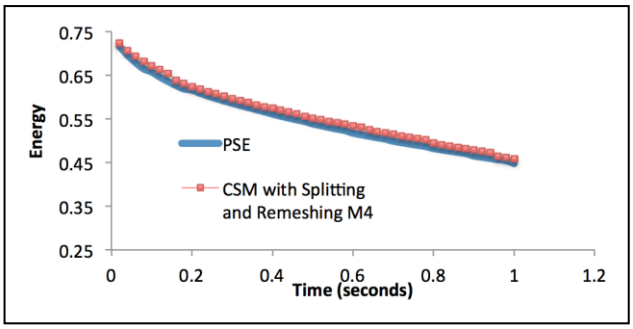

Figure 6 Comparison of the history of kinetic energy versus time between CSM and PSE.

During time evolution from 0 to 1, the energy decay calculated by CSM (red-dashed line) agreed very well with that of PSE (solid line). However, the figure also shows that the results from PSE were more dissipated than those from CSM. It is quite possible that the change of the core threshold from σ_{max} to $0.9.\sigma_{max}$ in CSM has some effect on the decay process of the energy spectrum. In other words, constraining the particles' core to $\alpha.\sigma_{max}(0 < \alpha < 1.2)$ has a significant effect on the decay rate of kinetic energy.

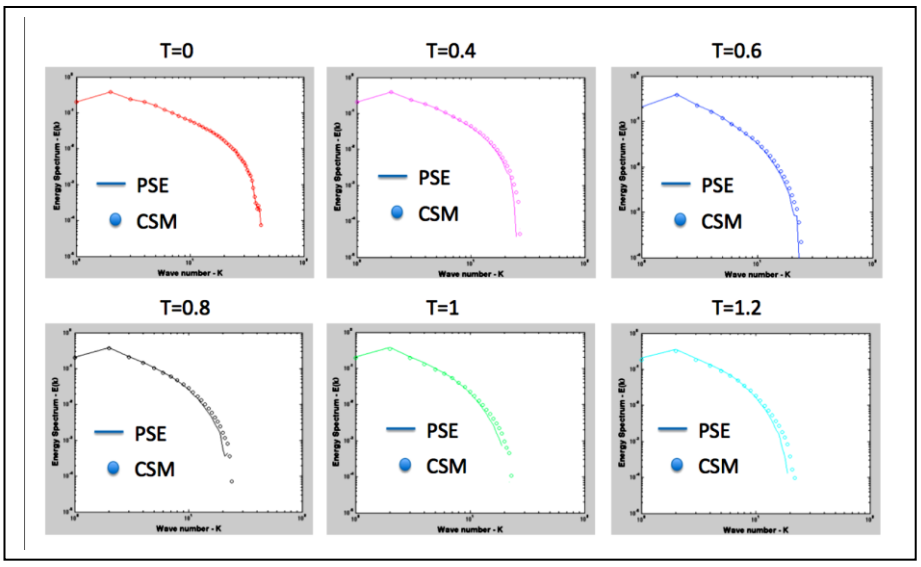

Figure 7 Comparison of evolution of the energy spectrum in wavenumber space between the CSM method (dotted circle) and the PSE method (continuous line).

The significant influence of the diffusion models on the dissipation process can

be clearly seen by plotting the energy spectrum vs. wave number, as depicted in Figure 7. In the figure, the CSM calculations (dashed line) approach the PSE results (solid line) within the energy-containing range (low wave numbers). This is not surprising because both simulations used the same initial conditions and boundary conditions (specifically for the vortex blob's core). The same behavior between CSM and PSE results can be observed within the inertia sub-range from T=0 (second) to T=1.2 (second). However, the PSE calculations deviate from those calculated using CSM in the dissipation range (high wave number region).

The results demonstrate that the present CSM performs better than PSE within the dissipation range because the core evolution of the particle in CSM actually expanded the dissipation range. This is probably due to the fact that the particle core in CSM is controlled to be smaller than in PSE during the time evolution. Accordingly, the dissipation process is improved at higher wave numbers as the simulation time increases.

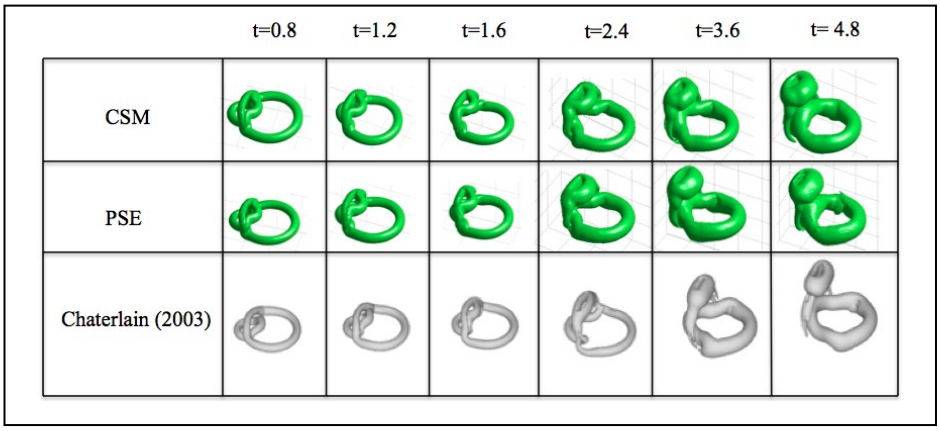

Figure 8 The isosurface evolution of vorticity contours.

In order to look at the details of the reconnection process during the collision of the two vortex rings, the isovorticity contours' evolution is plotted in Figure 8. The CSM simulation results were compared with those simulated using PSE and those from Chaterlain. The vorticity evolution is presented from t=0.8 to t=4.8. The results show that there is only a small difference between the CSM results and the PSE results. Furthermore, the CSM results agree very well with those reported by the reference. Therefore, it can be concluded that the developed CSM-based vortex method performs very well in simulating unbounded flows.

Figure 9 shows the isosurface of the second invariant of the velocity gradient tensor $Q = 0.5 \times tr(\nabla u_{ij} \nabla u_{ij})$ at time T=4.8. Fig. 9 (a) is the isosurface from PSE. Fig. 9 (b) is the isosurface from CSM. Fig. 9 (c) is the isosurface of the difference of Qbetween both methods. The results show that the larger structures of the current CSM match those of PSE, while the smaller structures of the two methods still behave differently. The same behavior can also be observed in Figure 7, where the kinetic energy at higher wave numbers does not match.

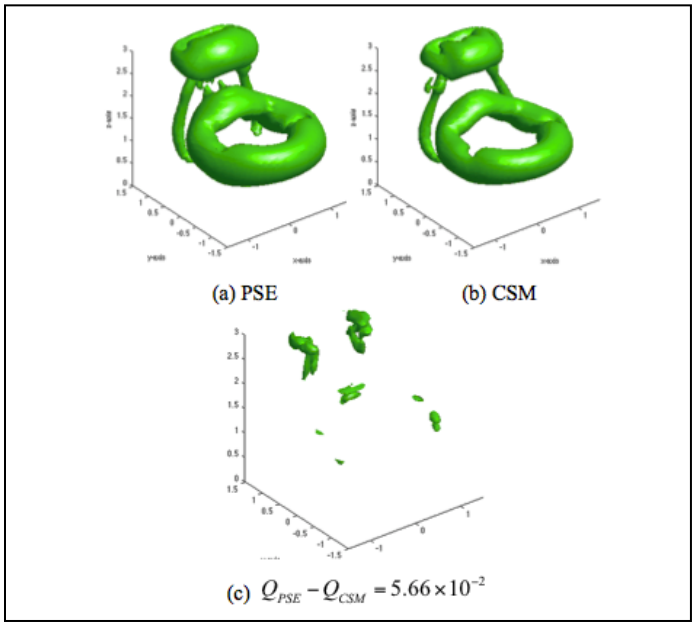

Figure 9 Isosurface of second invariant of velocity derivative tensor.

3.2 Simulation of flow past an impulsively started sphere at Re=100

Simulations of flow past an impulsively started sphere were conducted in order to investigate the performance of the developed code in simulating 3D bounded flows. The flow past an impulsively started sphere is a benchmark test for bounded flow simulation and has been investigated numerically and experimentally by many authors for Reynolds numbers from 0.5 to several thousands. In the context of numerical methods, the incompressible vortical flow around a sphere at low Reynolds numbers (from 10 to 300) has been simulated using botha particle method (Kim [17] – vortex-in-cell method) and a grid-based method (Johnson and Patel [18]). In addition, this type of external flow simulation nowadays has become a popular testing case for the

enforcement of no-through and no-slip boundary conditions. This is because the flow remains laminar at the low Reynolds numbers, whereas the statistics of the flow are stationary stable and can be neglected, specifically in the near-wall region.

In this work, flows past a sphere at Re=100 was simulated in order to test the performance of the proposed CSM's diffusion model. The results of the simulation were compared with the numerical solutions of Kim [17], Johnson and Patel [18], and Taneda [19]. In this simulation, a sphere with radius 0.5 was discretized into triangular panels (the number of panels was 1280 and the number of vertices was about twice that of the panels). The free stream velocity is set to $U_\infty = 1, V_\infty = 1, W_\infty = 1$. The time step for the simulation was set to be $\Delta t = 0.025$.Figure 10 depicts the reported variation of the drag coefficient, C_D, versus the Reynolds numbers for flow around a sphere.

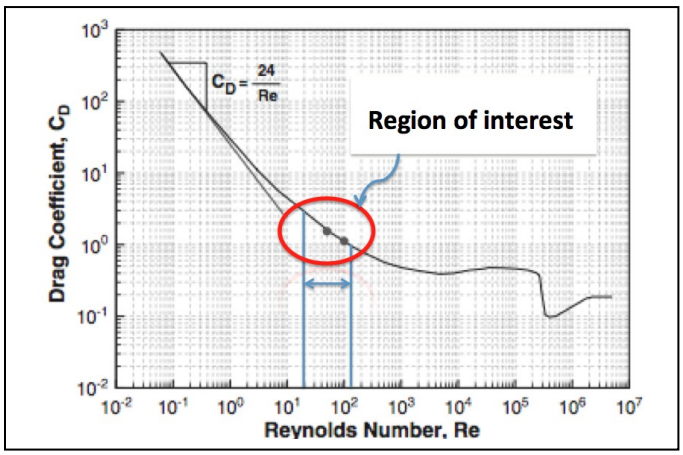

Figure 10 Drag coefficient C_D versus Reynolds numbers of flow around a sphere [17].

Figure 11 shows the streamlines (left side) and vorticity contour (right hand side) calculated using the developed CSM code. These plots illustrate quantitatively the development of a symmetrical wake behind the sphere from the initial stage until the later stages of the simulation (T=7.5). As depicted in the figure, a pair of vortex bubbles steadily developed into larger and larger bubbles during simulation time. As can clearly be seen in the vorticity contour plot, the separation point is found to be located around 60^o, which agrees well with the numerical result of Kim and the experimental result of Taneda.

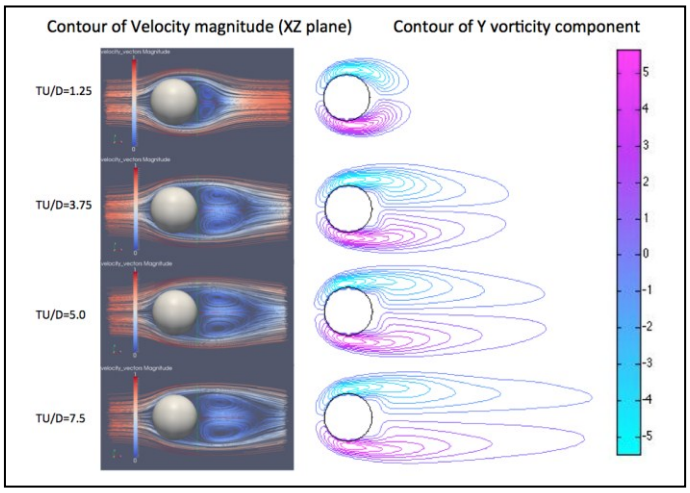

Figure 11 Left: Contour of Velocity magnitude in XZ plane. Right: Contour of vorticity in XZ plane.

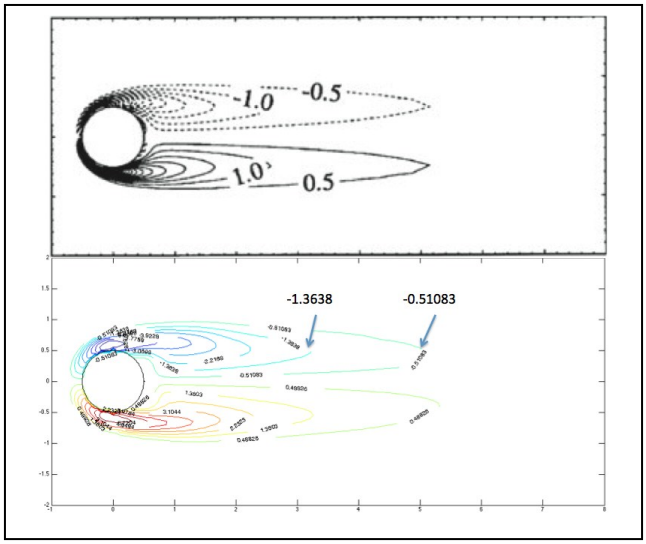

Figure 12 Comparison of vorticity contours of the flow past a sphere at Re = 100 (the upper is the result from Johnson and Patel, the lower is the result from the present method).

Figure 12 depicts the instantaneous vorticity contours at simulation time T=7.5. The result from the present method (lower plot) is compared with the grid-based result from the simulation conducted by Johnson and Patel (upper plot). The difference between the downstream extension of the vorticity contour calculated using the present method and the reference appears to be very small. Therefore,

it can be concluded that the circulation zone surrounding the sphere simulated using the present CSM agrees very well with the results from Johnson and Patel.

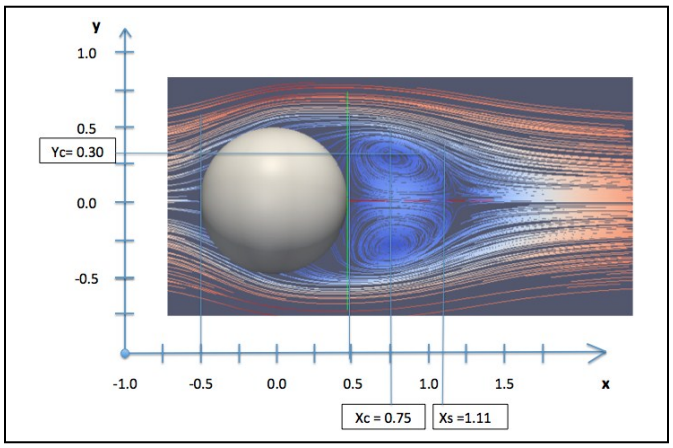

Figure 13 Evaluation of the center of the vortex bubble behind the sphere

Figure 13 shows the measurement of the position and the length of the dynamic vortex bubbles that steadily developed behind the sphere. A comparison of the position and the length of the vortex bubble computed using the present CSM with the results from Kim and Johnson, will determine the accuracy of the implementation of the boundary conditions in the present method.

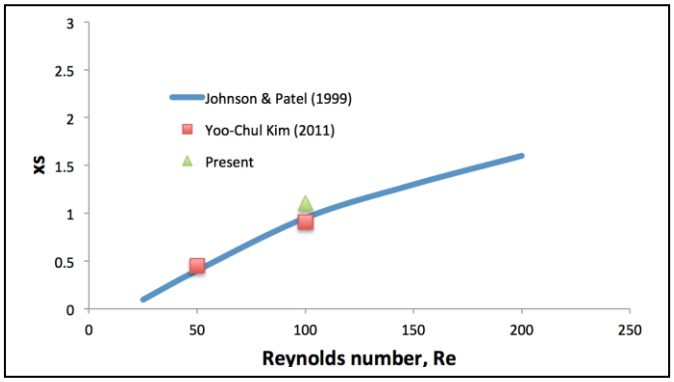

Figure 14 Length of the Vortex bubble from the present CSM compared to that of other numerical methods.

Figure 14 and 15 compare the length and position of the bubble center calculated using the current CSM method with those from the references.

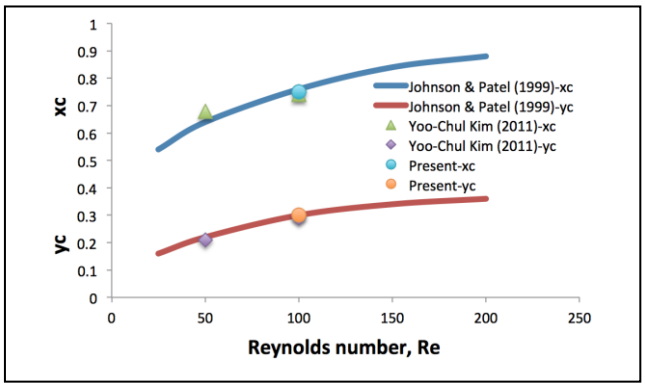

Figure 15 Position of the Vortex bubble's center from the present CSM compared to that of other numerical methods.

These figures show a good agreement between the present CSM's results with the results of Johnson and Patel and Kim. Furthermore, as shown in Figure 14, there is a small difference between the length of the vortex bubble calculated using the present method with the results from Johnson and Patel and Kim. This difference is due to the fact that the convection error of the vortex blob velocities is reduced in the flow simulation due to the spatial adaptation process. In fact, the error comes from the fact that continuous spreading of the vortex blobs' core radius in CSM occurs without the consideration of controlling the core size. As the core size increases, the vortex blobs no longer move with their actual local velocity. However, this error is relatively small, which shows that the current implementation of the boundary conditions works very well. Therefore, it can be concluded that the developed CSM's diffusion model performs very well in simulating external flow around a complex body at small or even moderate Reynolds numbers.

4 Conclusions

An algorithm for a CSM-based vortex method, with a splitting spatial adaptation scheme, which employs theM_4'remeshing scheme, was developed. For unbounded flow, the simulation of a vortex ring using the CSM diffusion model with M_4' spatial adaptation produced a kinetic energy and energy spectrum that agreed well with the reference calculation using PSE. However, comparison of the isosurface of the second invariant of the velocity derivative tensor showed that while the larger structures produced by the proposed CSM match those of PSE, there are still slight variations in the smaller structures produced. For bounded flow, the developed CSM diffusion model performs very well in simulating the 3D external flow around an impulsively started sphere at small or even moderate Reynolds numbers. Comparison of the

position and length of the vortex bubble calculated using the proposed CSM with those obtained in previous studies demonstrated the accuracy of the implementation of the boundary conditions in the present method. In the near future, the developed method will be used to simulate the flow around a bluff body at higher Reynolds numbers, as well as to simulate flows around more complex boundaries.

Acknowledgements

The authors would like to gratefully thank AUN/SEED-Net for supporting this research through project No. ITB CR 1301.This research was also partially supported by ITB Research and Innovation Grant 2014.

References

[1] Rasmussen, T.R., *A Penalization Interface Method for 3D Particle Vortex Methods*, Master Thesis, Mechanical Engineering, Technical University of Denmark, Lyngby, 2008.

[2] Li, G., Müller, U.K., van Leeuwen, J.L. & Liu, H., *Body Dynamics and Hydrodynamics of Swimming Fish Larvae: a Computational Study*, Journal of Experimental Biology, **215**, pp. 4015-4033, 2012.

[3] Mattia, G., Chatelain, P., Rees, W.M. & Koumoutsakos, P., *Simulations of Single and Multiple Swimmers With Non-Divergence Free Deforming Geometries*, Journal of Computational Physics, **230**, pp. 7093-7114, 2011.

[4] Eric, D.T., *The Hydrodynamics of Eel Swimming II. Effect of Swimming Speed*, Journal of Experimental Biology, **207**, pp. 3265-3279, 2004.

[5] Kajtar, J.B. & Monaghan P.P., *On The Swimming of Fish-Like Bodies Near Free and Fixed Boundaries*, European Journal of Mechanics – B/Fluids, **33**, pp. 1-13, 2012.

[6] Barba, L.A., *Vortex Method for Computing High-Reynolds Number Flows: Increased Accuracy with a Fully Mesh-less Formulation*, PhD Dissertation, Department of Aeronautical Engineering, California Institute of Technology, California, 2004.

[7] Cottet, G.H. & Poncet, P., *Advances in Direct Numerical Simulations of 3D Wall-Bounded Flows by Vortex-In-Cell Methods*, Journal of Computational Physics, **193**, pp. 136-158, 2004.

[8] Kamemoto, K., *On Contribution of Advanced Vortex Element Methods Toward Virtual Reality of Unsteady Vortical Flows in the New Generation of CFD,* Brazilian Congress of Thermal Sciences and Engineering, **26**, pp. 368-378, 2005.

[9] Ploumhans, P. & Winckelmans, G.S., *Vortex Methods for High-Resolution Simulations of Viscous Flow Past Bluff Bodies of General Geometry*, Journal of Computational Physics, **165**, pp. 354-406, 2000.
[10] Greengard, C., *The Core-Spreading Vortex Method Approximations The Wrong Equation*, Journal of Computational Physics, **61**, pp. 345-348, 1985.
[11] Yokota, R., *Validation of Vortex Methods as a Direct Numerical Simulation of Turbulence*, PhD Dissertation, Mechanical Engineering, Keio University, Yokohama, 2009.
[12] Rossi, L., *Merging Computational Elements In Vortex Simulations*, SIAM Journal on Scientific Computing, **18**, pp. 1014-1027, 1997.
[13] Rossi, L., *Resurrecting Core-Spreading Vortex Methods: a New Scheme That is Both Deterministic and Convergent*, SIAM Journal on Scientific Computing, **17**, pp. 370-397, 1996.
[14] Huang, M.J., Su, H.X. & Chen, L.C.,*A Fast Resurrected Core-Spreading Vortex Method with No-Slip Boundary Conditions*, Journal of Computational Physics, **228**, pp. 1916-1931, 2005.
[15] Greengard, L. & Rokhlin, V., *A Fast Algorithm for Particle Simulations*, Journal of Computational Physics, **73**, pp. 325-348, 1987.
[16] Chatelain, P., *Reconnection of Colliding Vortex Rings*, Physical Review Letter, Department of Aeronautical Engineering, California Institute of Technology, California, 2003.
[17] Kim, Y.C, *Vortex-In-Cell Method Combined with a Boundary Element Method for Incompressible Viscous Flow Analysis*, International Journal of Numerical Methods in Fluids, **69**, pp. 1567-1583, 2011.
[18] Johnson, T.A. & Patel, V.C., *Flow Past a Sphere Up To Reynolds Number of 300*, Journal of Fluid Mechanics, **378**, pp. 19-70, 1999.
[19] Taneda, S., *Studies on Wake Vortices (III). Experimental Investigation of the Wake behind a Sphere at Low Reynolds Number*, Reports of Research Institute of Applied Mechanics, **4**, pp. 99-105, 1956.